A Mesoporous Pt/TiO_2 Nanoarchitecture with Catalytic and Photocatalytic Functions

Xinchen Wang,[a] Jimmy C. Yu,*[a, b] Ho Yin Yip,[a, c] Ling Wu,[b] Po Keung Wong,[a, c] and Suk Yin Lai[d]

Abstract: A novel metal/semiconductor nanocomposite with catalytic and photocatalytic functions has been prepared. The new material consists of highly dispersed platinum (Pt) nanoparticles embedded in a cubic mesoporous nanocrystalline anatase (meso-nc-TiO_2) thin film. The porous thin film possesses a narrow pore-size distribution and a large surface area. The diameter of the Pt cluster can be controlled to below 5 nm, and the high dispersion of these clusters gives rise to catalytic activity for the oxidation of carbon monoxide, an important reaction for automobile exhaust treatment. This novel ordered mesoporous Pt/TiO_2 nanoarchitecture is also a promising photochemical material, as demonstrated by the photo-driven killing of *Micrococcus lylae* cells on the film.

Keywords: heterogeneous catalysis · mesoporous materials · photocatalysis · platinum · thin films

Introduction

Small metal particles dispersed on high-surface-area metal oxides have attracted much attention because of their extraordinary catalytic and optical/electronic properties. These properties are attributable to surface effects, quantum-size effects, and metal–support interactions.[1] Advances in physical methods for characterizing such metal–support nanocomposites have led to a molecular-level understanding of the structure–performance relationships that are strongly related to the size, shape, and surface structure, as well as the bulk and surface compositions of the composites.[1] This knowledge, together with novel approaches to nanostructural fabrication, has inspired the design and development of new composites for advanced applications.

Among various materials, noble-metal/active-oxide composites such as Pt/TiO_2 are most attractive.[1b–d,2] They are a classic example of catalysts in which the catalytic properties of the metal component are strongly modified by interaction with the active oxide support. This nanocomposite not only retains the catalytic activity of metal nanoparticles, but also possesses the intrinsic photocatalytic capacity of TiO_2. Moreover, the deposited Pt particles have been demonstrated to serve as trapping centers for electrons generated in light-activated TiO_2, leading to an improved quantum efficiency for photochemical reaction systems.[3]

The metal/semiconductor composites are generally prepared by impregnation,[4] ion exchange,[5] co-precipitation,[6] deposition–precipitation,[7,4c] vapor-phase deposition, and grafting.[8] In addition, recent advances in nanosynthetic chemistry offer unexplored opportunities for the creation of novel nanocomposite systems. For example, core-shell nanostructures of metal/oxide composites have been fabricated.[9] Very recently, Agostiano and co-workers[10] reported soluble semiconductor/metal nanocomposites, in which the authors employed anatase-TiO_2 nanorods to stabilize silver nanoparticles in a homogeneous nonpolar solution. The self-assembly approach to ordered mesoporous oxides[11] initiated by Mobil Corp. scientists has also sparked interest in the syn-

[a] X. Wang, Prof. Dr. J. C. Yu, H. Y. Yip, Prof. Dr. P. K. Wong
Environmental Science Programme
The Chinese University of Hong Kong
Shatin, New Territories, Hong Kong (China)
Fax: (+852) 2603-5057
E-mail: jimyu@cuhk.edu.hk

[b] Prof. Dr. J. C. Yu, L. Wu
Department of Chemistry
The Chinese University of Hong Kong
Shatin, New Territories, Hong Kong (China)

[c] H. Y. Yip, Prof. Dr. P. K. Wong
Department of Biology
The Chinese University of Hong Kong
Shatin, New Territories, Hong Kong (China)

[d] Prof. Dr. S. Y. Lai
Department of Chemistry
Hong Kong Baptist University
Kowloon, Hong Kong (China)

Supporting information for this article is available on the WWW under http://www.chemeurj.org/ or from the author.

 DOI: 10.1002/chem.200401248

thesis of metal/oxide composites. This approach could produce mesostructured titania in both bulk and thin-film forms.[12] These periodic porous TiO_2 materials can be viewed as a regular ensemble of individual TiO_2 nanocrystals sintered together to establish an electronic semiconducting network with periodic cavities and channels. Such a zeolite-like mesoporous nanocrystalline TiO_2 should be a superior host for supporting metal particles because: 1) the regular nanopore arrays in the meso-nc-TiO_2 matrix provide a constrained microenvironment for the production of highly dispersed metal nanoparticles and 2) the nanoparticles thus formed are confined in the small volume and are stabilized by the mesonetwork itself, thus eliminating the requirement for potentially catalyst-poisoning organic ligands for stabilization.[13] Moreover, the meso-nc-TiO_2 molecular-sieve host matrix also provides beneficial effects for photochemical applications. This is because it can enhance the light-harvesting ability of the Pt/TiO_2 composite due to its large external surface area and multiple scattering effects, and additionally, because it can allow highly efficient electron transport through the networks of interconnected TiO_2 nanocrystal arrays.[14]

In this paper we report on the fabrication of Pt nanoparticles in the pore channels of mesostructural TiO_2 thin films. X-ray diffraction (XRD), transmission electron microscopy (TEM), scanning electron microscopy (SEM), X-ray photoelectron spectra (XPS), and N_2 sorption were employed to characterize the resulting material. Catalytic and photocatalytic functions of the mesoporous Pt/TiO_2 nanocomposite were examined by the oxidation of CO and the destruction of bacteria, respectively.

Results and Discussion

Synthesis of the porous Pt/TiO_2 nanoarchitecture: A newly developed sono- and photochemical approach[15] was used to prepare highly dispersed platinum nanoparticles in the meso-nc-TiO_2 matrix. This approach involves two steps. First, a TiO_2 film was immersed in a solution of $PtCl_4$ in water and irradiated by ultrasound under reduced pressure. The sonication significantly increases the intrinsic mass-transfer coefficient and effective diffusivity in a solid–liquid system by creating high-speed microscopic turbulence at their interface.[16] This microturbulence effectively drives the liquid into the porous matrix,[17] producing a homogeneous distribution of the ionic Pt precursors throughout the film. Then, upon UV irradiation, the Pt ions were reduced to Pt nanoparticles by TiO_2 photocatalysis in the presence of methanol. The nanoparticles are confined by the nanosized pores, thus eliminating the need for potentially catalyst-poisoning organic ligands for stabilization.

Mesostructure and crystal structure of the pore wall: Figure 1 displays the low-angle XRD (LXRD) patterns of the as-synthesized TiO_2, calcined mesoporous TiO_2 (MT), and Pt-deposited mesoporous TiO_2 (Pt-MT) films. The

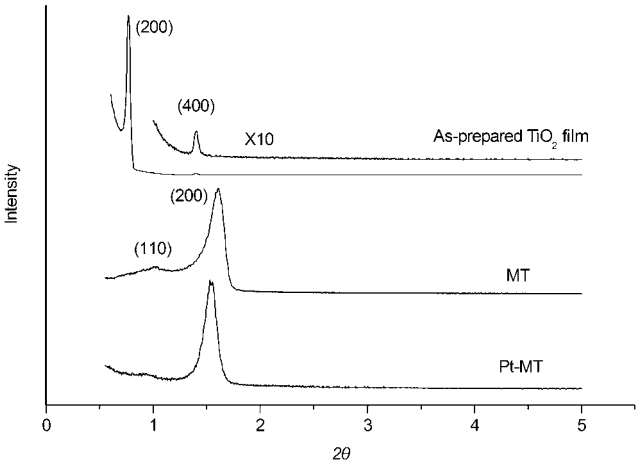

Figure 1. Low-angle XRD patterns of the as-prepared TiO_2, MT, and Pt-MT thin films.

LXRD of the as-synthesized TiO_2 film exhibits two peaks assigned to a cubic symmetry. The intense and narrow peaks suggest a very highly organized and oriented mesostructure. The peaks can be indexed as the (200) and (400) reflections associated with the $Im\bar{3}m$ symmetry with the {100} lattice planes of the unit cell oriented parallel to the substrate. It is noted that the disappearance of the (110) reflection is due to the oriented nature of the film. Similar results have also been reported by Stucky and co-workers[18] for an oriented-growth mesoporous TiO_2 film with a body-centered cubic mesostructure. After calcination, the intense (200) peak still remains, but shifts from 0.75 to 1.61° due to shrinkage. As a result, the value of the cell lattice parameter, a, is shifted from 230 to 109 Å. Judging from the Thermogravimetry/Differential Thermal Analysis (TG-DTA) data (see the Supporting Information), the shrinkage was due to the removal of HCl and surfactant, as well as the densification of the TiO_2 wall during the thermal treatment. In addition, after calcination, a relatively weak peak assigned to the (110) reflection of the cubic mesostructure appeared. This, together with TEM measurements (see the Supporting Information), confirms the $Im\bar{3}m$ symmetry of the sample. Such a cubic ordered mesoporous TiO_2 film with robust inorganic pore-wall structure may provide a superior host matrix for encapsulating guest species. After the inclusion of platinum particles, the resulting Pt-MT composite film shows similar LXRD patterns to those of the MT film, indicating that the incorporation of platinum particles does not destroy the mesostructural ordering.

Figure 2 shows the wide-angle XRD patterns of the MT and Pt-MT films. Both samples exhibit four distinct peaks contributed by anatase-TiO_2 (JCPDF 21-1272). The average anatase-TiO_2 particle size was approximately 6 nm, as estimated from the peak width of the anatase (101) reflection by using the Scherrer equation with a spherical model for approximation.[19] Such a nanocrystalline pore-wall structure partially explains the stability of the mesostructure during

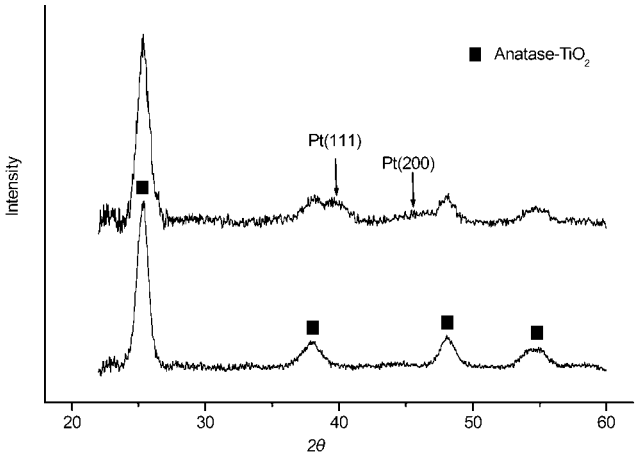

Figure 2. Wide-angle XRD patterns of the MT and Pt-MT thin films.

the sonochemical processing. Close examination of the peaks in MT and Pt-MT films reveals that two weak but resolvable peaks occurred for the Pt-MT sample. The peaks can be attributed to the (111) and (200) reflections of the Pt^0 (JCPDF 01-1194) possessing a face-centered cubic structure with an *Fm*3*m* space group. These peaks are weak and broad, indicating the nanocrystalline nature of the platinum particles encapsulated in the films.

Morphology and particle size: The TEM image taken in the (111) direction of the Pt-MT film (Figure 3a) clearly shows that the platinum nanoclusters are highly dispersed in the framework of well-ordered MT. The appearance of Pt particles in the (111) plane of the $Im\bar{3}m$ mesostructured TiO_2 film gives direct evidence that the nanoparticles are effectively encapsulated in the skeleton instead of on the surface of the film. As shown in Scheme 1, the (111) plane is located in the bulk of the orientationally grown film with {100} lattice planes parallel to the substrate. The TEM results also suggest that the cubic interconnected mesoporous framework is extended throughout the film and thus is fully accessible from the surface. This is a particularly important property for maintaining a fast mass-transfer throughout the porous architecture.

Energy dispersive X-ray (EDX) measurements (Figure 4) reveal a composition of ~1 atomic% of Pt in the film. A representative high-resolution TEM (HRTEM) image (Figure 5) confirms that the Pt nanoparticles are embedded in the nanocrystalline mesoporous TiO_2 framework. The particle size of Pt, as estimated form HRTEM images, is 1–5 nm, which is compatible with the pore diameter (3–7 nm) of the MT host (shown in the N_2 sorption results). The platinum nanocrystals are confined in the pores, and are surrounded by TiO_2 nanocrystals embedded in the pore wall. The lattice fringes of $d = 3.3$ and 2.0 Å match that of the (101) and (200) crystallographic planes of anatase-TiO_2 and Pt cubic phase, respectively, thus confirming the existence of Pt || TiO_2 nanocontacts.

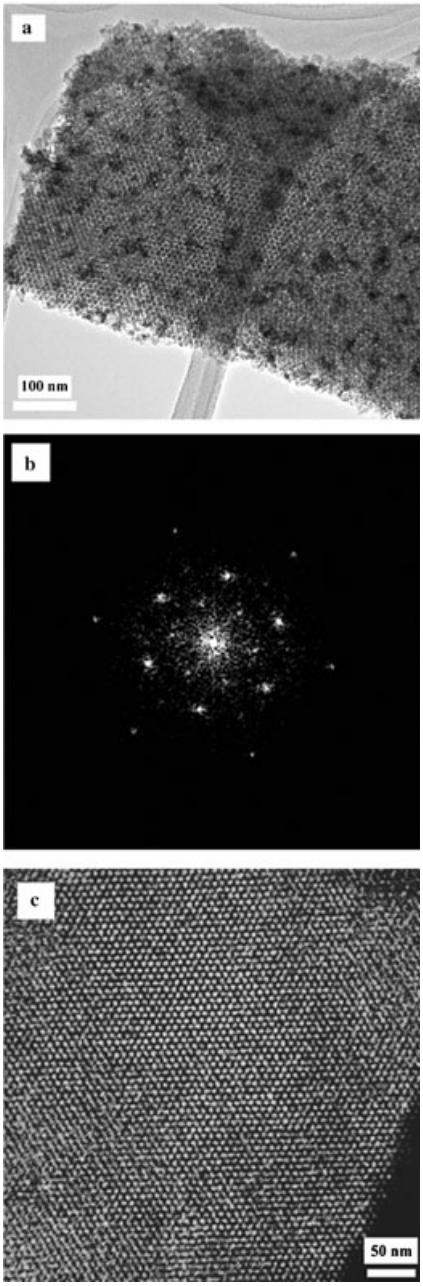

Figure 3. TEM images of a) Pt nanoclusters confined in TiO_2 mesonetwork viewed along the (111) direction, with b) corresponding Fourier transform of the full image, and c) pure MT film as a comparison.

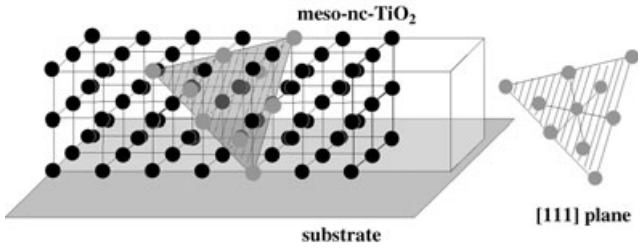

Scheme 1. The body-centered cubic meso-nc-TiO_2 film with [100] lattice planes parallel to the substrate. The [111] lattice planes are located in the bulk of the mesostructured film.

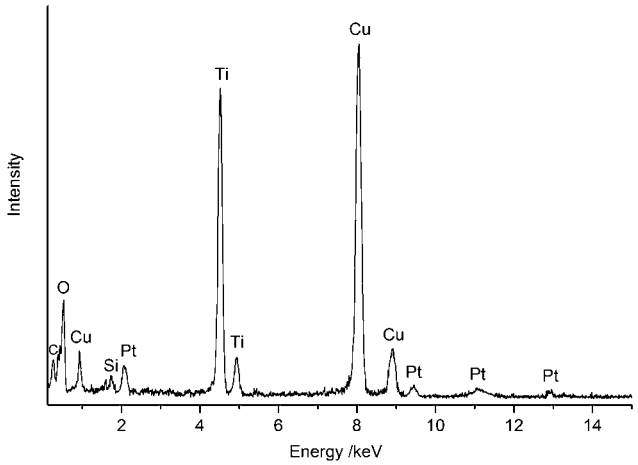

Figure 4. EDX results corresponding to Figure 3a (Cu and C come from the supporting carbon-coated copper grid, and the Si comes from the substrate).

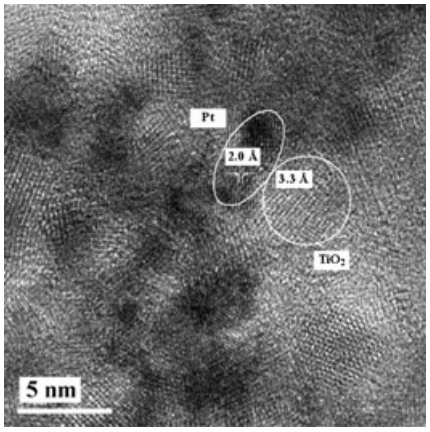

Figure 5. A representative HRTEM image of the Pt and TiO_2 nanoparticles in the Pt-MT thin film. The dark particles represent Pt, and the gray particles are TiO_2. The Pt/TiO_2 nanoheterojunctions are clearly shown in the image.

N_2 adsorption analysis: Figure 6 shows nitrogen adsorption–desorption isotherms and Barrett–Joyner–Halenda (BJH) pore-size distribution plots of the MT and Pt-MT samples. Both samples show similar type-IV isotherms, which are representative of mesoporous solids.[20] The BJH pore-size analyses performed on the adsorption branch show that both samples exhibit nearly identical pore-size distribution plots. A narrow pore-size distribution ranging from 3 to 7 nm with a maximum at ~4 nm is evident for the MT and Pt-MT samples. The specific surface area of each sample, calculated by the multi-point Brunauer–Emmett–Teller (BET) method, is 189 $m^2 g^{-1}$ for MT and 185 $m^2 g^{-1}$ for Pt-MT. These values are quite large considering their large pore diameter. As no systematic change in either the shape of the sorption isotherms or in the specific surface area was found, the incorporation of the Pt nanoparticles does not appear to destroy the mesoporous structure and to alter the sorption properties of small molecules such as N_2. These observations likely arise from 1) the relatively small number of nanoparticles that are contained within the materials and 2) the fact that the particle size is smaller than the parent pore channels. In addition, for the Pt-MT film, after loading of platinum particles, the pore volume and pore diameter decrease from 0.261 to 0.249 $cm^3 g^{-1}$ and from 40.1 to 39.6 Å, respectively, with a slight decrease of porosity from 48.2 to 47.5 % (see Table 1). These decreases, along with the increased thickness

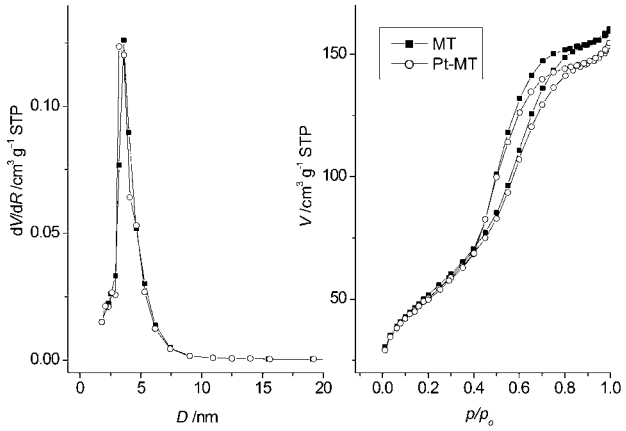

Figure 6. Pore size distribution plots (left) and N_2 adsorption-desorption isotherms (right) for the MT and Pt-MT samples.

Table 1. Pore-wall parameters of the MT and Pt-MT films calculated from the X-ray diffraction results (Figure 2) and the N_2 sorption isotherms (Figure 6).

Sample	S_{BET}[a]	V[b]	D_{BJH}[c]	Porosity[d]	$d_{(100)}$[e]	Wall thickness[f]
	[$m^2 g^{-1}$]	[$cm^3 g^{-1}$]	[Å]	[%]	[Å]	[Å]
MT	189	0.261	40.1	48.2	108.8	68.7
Pt-MT	185	0.249	39.6	47.5	112.2	72.6

[a] BET surface area calculated from the linear part of the BET plot (P/P_0 = 0.1–0.2). [b] Total pore volume, taken from the volume of N_2 adsorbed at P/P_0 = 0.995. [c] Average pore diameter, estimated using the desorption branch of the isotherm and the Barrett–Joyner–Halenda (BJH) formula. [d] The porosity is estimated from the pore volume determined using the adsorption branch of the N_2 gas isotherm curve at P/P_0 = 0.995. [e] $d_{(100)} = 2 d_{(200)}$. [f] Wall thickness = $d_{(100)} - D_{BJH}$.

of pore wall from 68.7 to 72.6 Å, can be attributed to the inclusion of Pt nanoclusters into the pore channels of the MT film.[21] The slight decrease also suggests that most of the nanometer-sized pore channels of the host MT film are open, although a small portion of the channels may be filled with the Pt particles. The open-pore channels are very important for the permeation of reactant molecules and photocatalytic active species in the porous systems.

Surface electronic states and composition: The surface electronic states of the sono-deposited Pt nanoparticles in TiO_2 were studied by XPS. The peaks at 72.2 and 75.4 eV in

trace a of Figure 7 are assigned to $Pt(OH)_2$.[22] This confirms the effective conversion of the Pt^{IV} precursor to Pt^{II} under ultrasound irradiation. It is known that sonication can induce the formation of reductive $H^{\cdot}$ species.[23] The $PtCl_4$ precursor is reduced to Pt^{II} and then subsequently reacts with surface hydroxyl groups in the porous TiO_2 network to form $Pt(OH)_2$. The binding energy decreases when the $Pt(OH)_2$-adsorbed MT film is exposed to UV light. The peaks at 70.4 and 73.7 eV in trace b are assigned to elemental Pt. The change in the intensity ratio could be due to the presence of a trace amount of PtO on the Pt^0 nanoclusters. Nevertheless, the XPS results illustrate the effectiveness of the TiO_2 photocatalysis process in reducing $Pt(OH)_2$ to Pt^0. The formation of platinum nanoclusters may be represented by the reactions given in Equations (1)–(7) in which h = hole.

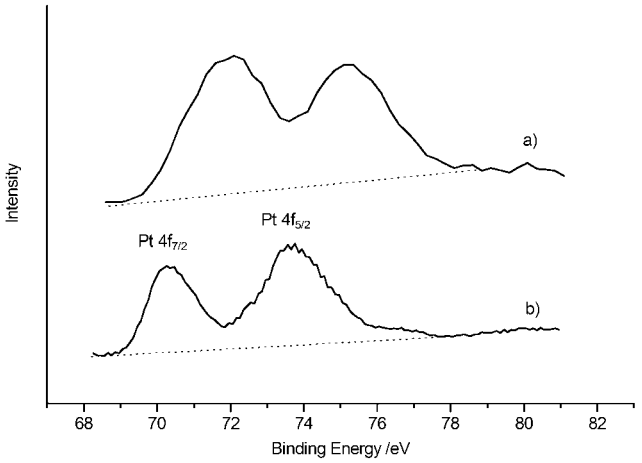

Figure 7. XPS spectra showing the Pt 4f peaks a) before and b) after UV irradiation.

$$H_2O \rightleftharpoons H^{\cdot} + HO^{\cdot} \text{ (sonication)} \quad (1)$$

$$Pt^{IV} + 2\,H^{\cdot} \rightarrow Pt^{II} + 2\,H^{+} \quad (2)$$

$$Pt^{II} + 2\,HO^{-}(\text{surface}) \rightarrow Pt(OH)_2 \quad (3)$$

$$TiO_2\ (UV) \rightarrow e^{-} + h^{+} \text{ (photocatalysis)} \quad (4)$$

$$Pt(OH)_2 + 2\,e^{-} + 2\,H^{+} \rightarrow Pt^0 + 2\,H_2O \quad (5)$$

$$n\,Pt^0 \rightarrow Pt_n{}^0 \quad (6)$$

$$CH_3OH + O_2 + 2\,h^{+} \rightarrow CO_2 + H_2O + 2\,H^{+} \quad (7)$$

It should be mentioned that the Pt $4f_{7/2}$ binding energy of 70.4 eV in Figure 7b is 1.0 eV lower than that of bulk atoms.[22] This may be explained by the formation of ultrafine Pt particles with a decreased coordination number of surface atoms. For such a decrease in coordination number, the binding energy would shift to lower values relative to the bulk value.[24] A similar effect was also observed by experiment for Pt[25] and Au,[15] as well as by calculations for Pd.[26] Another possible explanation of the low binding energy of the metal nanoparticles could be SMSI effects (strong support–metal interaction), which is a well-known phenomenon occurring in systems consisting of metal particles deposited on inorganic supports like TiO_2. It is noted that electronic charge transfer between Pt atoms and TiO_2 surface has been much studied in heterogeneous catalysis in order to understand the SMSI effect of noble-metal/TiO_2 systems. This system causes a Schottky diode behavior in Pt contacts on TiO_2.[27] Under these conditions, metallic Pt contacts evidently show electron-acceptor properties, because of the large work function of Pt contacts ($\varphi_{Pt} = 5.6$ eV).[27] Such electron-acceptor properties of Pt/TiO_2 Schottky diodes can significantly increase the quantum yield of TiO_2 photocatalysis by inhibiting the fast recombination of undesirable electron–hole pairs generated by UV illumination.[3]

Catalytic oxidation of carbon monoxide: Most metal catalysts prepared by chemical means often require stabilization and/or activation in oxygen or air at temperatures up to 400 °C. In this study, no calcination or reduction steps are needed because the deposited clusters are ligand-free. Thus, all the catalytic tests were performed on the fresh catalyst without further treatment.

Figure 8 shows the catalytic activities for CO oxidation as a function of temperature. The temperatures for 50 % (T50) and 90 % (T90) CO conversion are 186 and 233 °C, respectively. The reaction cycle, consisting of a heating and cooling period, was recorded to monitor possible deactivation or activation. Indeed, no modification of the catalytic activity was observed for the cycle, indicating the stability of the catalyst. The effect of time on the activity was also measured on the Pt-MT in order to check for possible deactivation. Two different measures were employed in this regard. First,

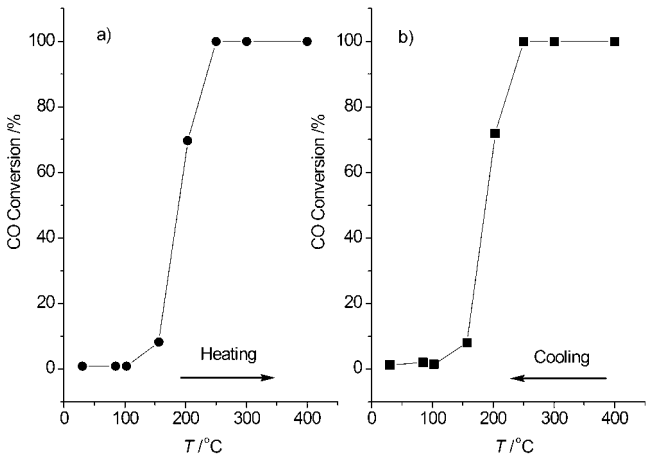

Figure 8. Temperature effect on CO oxidation on the Pt-MT catalyst for a) heating from 30 to 400 °C, and then for b) cooling from 400 to 30 °C.

immediately after the heating and cooling, the temperature was increased up to 180 °C under the reactive mixture and then kept constant for 5 h. Figure 9b shows that no deactivation occurred. The second measure was that the fresh catalyst was heated to 240 °C under a reactive atmosphere and then kept at steady-state conditions. As shown in Figure 9a, the sample showed no deactivation during time on stream. These results further confirm the physicochemical active state of the catalyst is stable even when exposed to thermodynamic forces such as temperature and reactive gas.

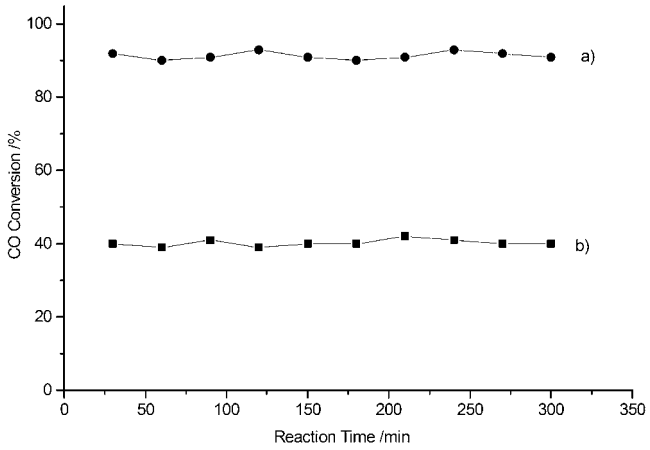

Figure 9. CO oxidation as a function of reaction time for a) the fresh Pt-MT catalyst at 230 °C, and for b) the used Pt-MT catalyst at 180 °C.

Photocatalytic activity in destroying *Micrococcus lylae* (*M. lylae*) cells: Figure 10 shows the percentage of cell survival after treatment with films activated by a 365 nm UV light. Significant cell death is observed only for the photoactivated Pt-MT film, with which 70 % of the *M. lylae* cells were killed in 60 min. The significant difference between MT and Pt-MT must be due to the interaction of the trapped Pt nanoclusters with the nanoanatase-TiO_2 host. The embedded Pt clusters could serve as trapping centers for electrons photogenerated in the conduction band (CB) of TiO_2, leaving the holes in the valence band (VB) of TiO_2.

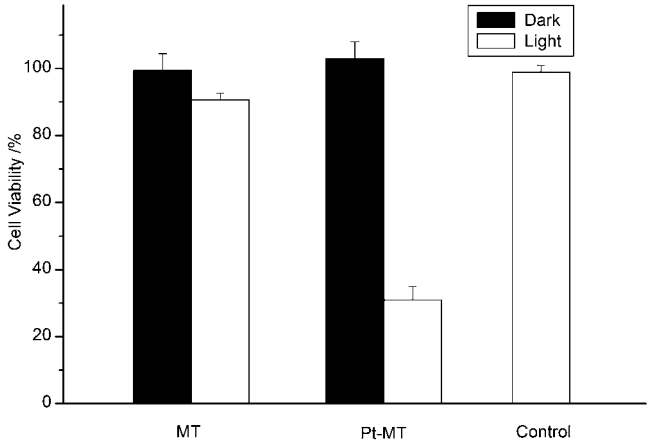

Figure 10. Percentage of cell survival of *M. lylae* on MT and Pt-MT films after irradiation with 365 nm UV light. The control experiment was carried out without the films.

Under the aerated conditions of our experiment, the dissolved O_2 trapped an electron from the Pt || TiO_2 nanoheterojunction, forming a superoxide anion radical ($O_2^{\bullet-}$), while the hole was captured by the surface-bound OH^- radical, producing a hydroxyl radical ($OH^{\bullet}$).[3] The $O_2^{\bullet}$ and $OH^{\bullet}$, together with subsequently generated $HO_2^{\bullet}$ and HOOH, are extraordinarily reactive oxygen species. These oxidative species can easily diffuse out of the porous matrix to attack the cells. As the photocatalyst would not directly attack the cells that were protected by an outer peptidoglycan layer,[28] the oxidative species are believed to be responsible for killing *M. lylae* cells. The photochemical processes are shown in Scheme 2, and the proposed initial elementary reactions are listed in Equations (8)–(15).

$$\text{Pt-TiO}_2\ (\text{UV}) \rightarrow \text{Pt}(e_{CB}^-) + \text{TiO}_2(h_{VB}^+) \quad (8)$$

$$\text{TiO}_2(h_{VB}^+) + OH^- \rightarrow OH^{\bullet} \quad (9)$$

$$\text{Pt}(e_{CB}^-) + O_2 \rightarrow O_2^{\bullet-} \quad (10)$$

$$O_2^{\bullet-} + H^+ \rightarrow HO_2^{\bullet} \quad (11)$$

$$2\,O_2^{\bullet-} + 2\,H^+ \rightarrow 2\,HO^{\bullet} + O_2 \quad (12)$$

$$HO_2^{\bullet} + H^+ + \text{Pt}(e_{CB}^-) \rightarrow H_2O_2 \quad (13)$$

$$H_2O_2 + \text{Pt}(e_{CB}^-) \rightarrow HO^{\bullet} + OH^- \quad (14)$$

$$(OH^{\bullet}, O_2^{\bullet-}, HO_2^{\bullet}, \text{HOOH}) + \text{cells} \rightarrow \text{damaged cells} \quad (15)$$

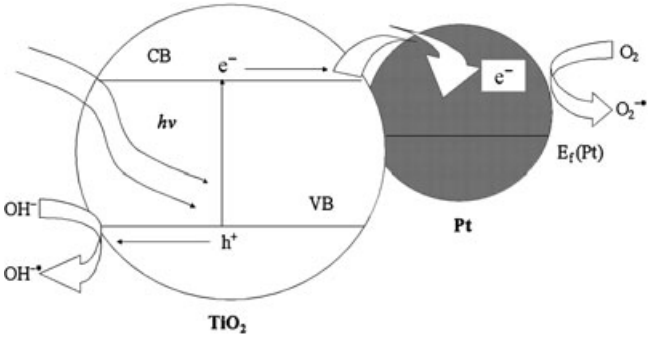

Scheme 2. Promoted charge carrier separation on Pt-MT photocatalyst by trapping a photoinduced electron on the Pt || TiO_2 junction.

The detailed bactericidal mechanism of these photocatalytically induced oxidative species is not unambiguously clear. However, based on our previous study on Ag/TiO_2 photocatalysts,[29] a possible bactericidal process can be proposed as follows. The plasma membrane can be first attacked by the oxidative species penetrating the outer layer of the bacteria. These reactive species can then oxidize coenzyme A and the plasma membranes. The oxidation of coenzyme A would inhibit cell respiration and directly cause cell death.[30] Meanwhile, the oxidation of the plasma membrane can break the main permeability barrier of the bacteria. This would result in the slow leakage of the intracellular materials including RNA, protein, and minerals, leading to

the subsequent death of *M. lylae*.[28] Detailed mechanism study on the bactericidal effect of TiO_2-based photocatalysis is still in progress.

Conclusion

Highly ordered mesoporous Pt/TiO_2 nanoarchitectures of high surface area and readily accessible to reactant molecules have been synthesized. The Pt clusters are encapsulated and stabilized in the robust pore channels of meso-nc-TiO_2 molecular sieve films, resulting in high dispersions of Pt nanoparticles. Such a Pt/TiO_2 composite can efficiently catalyze the oxidation of CO to CO_2. No deactivation during either heating or prolonged operation period was observed. These observations have illustrated the potential of Pt/TiO_2 composites as heterogeneous catalysts. Furthermore, the pore-stabilized Pt particles contact and interact with the anatase-TiO_2 nanocrystals embedded in the mesonetwork, forming semiconductor/metal nanoheterojunctions. These nanoheterojunctions promote the separation of charge carriers on UV-excited TiO_2,[3] thus significantly improving the photocatalytic activity of porous Pt/TiO_2 composites toward killing bacteria cells of *M. lylae*. This novel Pt/TiO_2 nanocomposite can also be potentially useful for many applications in sensors and environmental purification.

Experimental Section

Materials: All chemicals were used as-received without further treatment. Platinum chloride ($PtCl_4$, 99%), titanium tetraisopropoxide (Ti-(O*i*Pr)$_4$ or TTIP, 99%) were purchased from Aldrich. Triblock copolymer $(HO(CH_2CH_2O)_n\text{-}(CH_2CH(CH_3)O)_m\text{-}(CH_2CH_2O)_nH$, Pluronic P123, average $n/m = 20/70$, 99%) was kindly provided by BASF.

All solvents used were of analytical grade and purchased from Aldrich. Ultra-pure water was used in all experiments.

Preparation of samples: The mesoporous titania films were prepared by a surfactant-templated method in which TTIP was used as inorganic source and P123 was used as a structure-directing agent.[31] In a typical synthesis, a solution of TTIP (5.3 mL) in fuming HCl (2.7 mL, 37%) was added dropwise to a template solution prepared by dissolving P123 (1 g) in absolute ethanol (15 mL). The resulting clear colorless solution was stirred vigorously for 5 min at room temperature, and then aged at 4°C for another 5 min. The mother sol solution was used for dip-coating a glass substrate, quartz slide, or silicon wafer at a constant withdrawal rate (10 cm min^{-1}). The as-synthesized thin films were aged at 4°C for 24 h, and then aged again at room temperature for 1 h. The thin films were subsequently treated with NH_3 vapor for 5 s. After that, the films were heated at 60, 80, 120, and 200°C for 12 h, respectively. Calcinations were done in static air at 350°C (ramp rate of 1°C min^{-1}) and held for 4 h to remove the template and increase cross-linking of the inorganic framework. This resulted in continuous, transparent thin films with approximately 400 nm thickness as measured by an α-step profilometer. Alternatively, thick film samples were obtained by pouring the cool sol solution in a Petri dish to form a 1–2 mm thick liquid layer, followed by solvent evaporation and heat treatment. It is important that the surface of the Petri dish is flat in order to avoid phase segregation and inhomogeneity, resulting in a poorly structured mesophase product during drying.

The Pt-loaded TiO_2 thin film was obtained as follows: a calcined TiO_2 thin film was immersed in a bottle filled with a solution of metal precursor ($PtCl_4$, 20 mg) in deionized water (4 mL). The bottle was placed in an ultrasonic bath (Bransonic ultrasonic cleaner, model 3210EDTH, 47 kHz, 120 W, USA) and connected to a vacuum pump. After sonication under vacuum for 3 min, the film was stored in a vacuum oven for 12 h. The film was then washed gently with ultra-pure water to eliminate the surface-adsorbed precursor. After drying at 30°C under vacuum, the film was irradiated with UV light (254 nm, 10 mW cm^{-2}) in the presence of methanol vapor for 2 h, after which the film was washed by water to remove chloride ions. The amount of Pt can be controlled by using different concentrations of the precursors or by repeating the inclusion process.

Structural characterization

X-ray diffraction: LXRD diagrams were collected in θ-θ mode using a Bruker D8 Avance X-ray diffractometer ($Cu_{K\alpha 1}$ irradiation, $\lambda = 1.5406$ Å). Wide-angle XRD (WXRD) patterns were collected in parallel mode ($\omega = 0.5°$, 2θ varied from 20 to 60°, $Cu_{K\alpha 1}$ irradiation) using a Bruker D8 Avance X-ray diffractometer with a thin film optic. The crystallite size was estimated by applying the Scherrer equation to the fwhm (full width at half maximum) of the (101) peak of anatase, with silicon as a standard of the instrumental line-broadening. It is noted that repeated scanning is needed to increase the signal-to-noise ratio of WXRD measurements due to the small amount of thin film samples.

Transmission electron microscopy: Standard transmission electron microscopy (TEM) or high-resolution TEM (HRTEM) images were recorded on a JEOL 2010F microscope coupled with an electron dispersive X-ray (EDX) spectroscopic set-up. The system was used to study the morphology and composition of the films. Samples obtained by scratching the films from the substrates were suspended in methanol, followed by sonication for 5 min in the ultrasonic bath. Carbon-coated copper grids were used as the sample holders.

Nitrogen sorption: Nitrogen adsorption–desorption isotherms were collected at 77 K by using Micromeritics ASAP 2010 equipment (BET and BJH models for surface area and porosity evaluations, respectively) on samples scratched off the substrate. All the samples were degassed at 180°C and 10^{-6} Torr prior to the measurement.

X-ray photoelectron spectroscopy (XPS): XPS spectra were recorded on a PHI Quantum 2000 XPS System with a monochromatic $Al_{K\alpha}$ source and a charge neutralizer; all the binding energies were referenced to the C 1 s peak at 284.8 eV of the surface adventitious carbon.

Catalytic test

CO-oxidation: Catalytic tests were carried out at atmospheric pressure in a conventional fixed-bed reactor operated in single-pass mode. The gas mixture consisted of CO (1%), O_2 (20%), and N_2 (79%). Gases were mixed with mass flow controllers, by which reproducible $CO/O_2/N_2$ mixtures could be generated at a flow rate of typically 50 mL min^{-1}. The mixtures could then be sent either to the reactor or directly to the gas chromatograph for analysis.

The reactor was simply a Pyrex tube containing the Pt/TiO_2 sample (1.2 g) coated on quartz sand. The reaction cycle, consisting of a heating and a cooling period between 30 and 400°C, was recorded to monitor possible deactivation or activation. The reaction mixtures were analyzed by an on-line gas chromatograph equipped with a thermal conductive detector, and two columns with He as carrier gas. A Porapak Q column was used for the separation of CO and CO_2, and a 5 Å molecular sieve column for the separation of O_2 and N_2. Both columns were operated at 50°C. The usual procedure was used to verify that the activity was measured in the kinetic regime by varying the flow rate and the mass of catalyst in the same proportions to provide a constant contact time, and consequently a constant space velocity. The conversion did not vary as the mass flow was changed. This is an indication that the measured rate is not limited by external transfers (film diffusion). *T*50 and *T*90 are defined as the temperature at which the conversion of CO to CO_2 reached 50 and 90%, respectively.

Photo-driven bactericide (photocatalytic test)

Preparation of bacterial culture: *M. lylae*, a Gram positive bacterium that was isolated in our laboratory, was used as a model bacterium in the experiment. It was incubated in 10% trypticase soy broth (TSB) at 30°C with 200 rpm agitation for 24 h. The culture was washed with 0.9% saline

solution by centrifugation at 12000 rpm for 5 min at 25 °C, and the pellet was resuspended in saline. The cell suspension was adjusted in a centrifuge tube to the required cell concentration (3×10^5 cfu mL^{-1}).

Measurement of bactericidal activity: The photocatalyst film (1 cm × 2 cm) was immersed in saline solution (5 mL, 0.9 %) in a Petri dish. The dish was then sterilized by autoclaving at 121 °C for 20 min and, after cooling, was mixed with the prepared cell suspension. The final bacterial cell concentration was adjusted to 3×10^5 cfu mL^{-1}. The UV light was provided by a 15 W UV lamp. The intensity of the illumination was 0.15 mW cm^{-2} on the catalyst surface during the experiment. The photocatalytic reaction was started by irradiating the mixture with the light and stopped by switching off the light. Each set of experiments was performed in duplicate. The reaction mixture was stirred (220 rpm) with a magnetic stirrer. A bacterial suspension without photocatalyst was irradiated as a control and the reaction mixture without UV irradiation was used as a dark control. Before and after 1 h light irradiation, an aliquot of the reaction mixture was immediately diluted with saline solution (0.9 %) and plated on TSB agar. The colonies were counted after incubation at 37 °C for 48 h.

Acknowledgements

The work was supported by the Research Grants Council of the Hong Kong Special Administrative Region, China (Project No. CUHK 402904). The authors are indebted to Mr. Tze Kin Cheung of the Hong Kong University of Science and Technology for the TEM measurements and helpful discussions.

[1] a) M. Valden, X. Lai, D. W. Goodman, *Science* **1998**, *281*, 1647; b) D. R. Rolison, *Science* **2003**, *299*, 1698; c) A. T. Bell, *Science* **2003**, *299*, 1688; d) S. H. Joo, S. J. Choi, I. Oh, J. Kwak, Z. Liu, O. Terasaki, R. Ryoo, *Nature* **2001**, *412*, 169; e) Z. Xu, F. S. Xiao, S. K. Purnell, O. Alexeev, S. Kawi, S. E. Deutsch, B. C. Gates, *Nature* **1994**, *372*, 346.

[2] a) G. L. Haller, *J. Catal.* **2003**, *216*, 12, and references therein; b) A. Berko, J. Szoko, F. Solymosi, *Surf. Sci.* **2004**, *566*, 337; c) J. S. Lee, W. Y. Choi, *Environ. Sci. Technol.* **2004**, *38*, 4026; d) B. Sun, A. V. Vorontsov, P. G. Smirniotis, *Langmuir* **2003**, *19*, 3151; e) S. Kim, W. Choi, *J. Phys. Chem. B* **2002**, *106*, 13311; f) X. Y. Du, Y. Wang, Y. Y. Mu, L. L. Gui, P. Wang, Y. Q. Tang, *Chem. Mater.* **2002**, *14*, 3953; g) A. Hinz, P. O. Larsson, B. Skarman, A. Andersson, *Appl. Catal. B* **2001**, *34*, 161; h) D. R. Jennison, O. Dulub, W. Hebenstreit, U. Diebold, *Surf. Sci.* **2001**, *492*, L677; i) B. C. Trasferetti, C. U. Davanzo, R. A. Zoppi, N. C. Cruz, M. A. B. Moraes, *Phys. Rev. B* **2001**, *64*, 125404.

[3] M. R. Hoffmann, S. T. Martin, W. Choi, D. W. Bahnemann, *Chem. Rev.* **1995**, *95*, 69.

[4] a) V. Keller, P. Bernhardt, F. Garin, *J. Catal.* **2003**, *215*, 129; b) Y. L. Chen, D. Z. Li, X. C. Wang, X. X. Wang, X. Z. Fu, *Chem. Commun.* **2004**, 2304; c) G. R. Bamwenda, S. Tsubota, T. Nakamura, M. Haruta, *Catal. Lett.* **1997**, *44*, 83.

[5] a) H. R. Chen, J. L. Shi, Y. S. Li, J. N. Yan, Z. L. Hua, H. G. Chen, D. S. Yan, *Adv. Mater.* **2003**, *15*, 1078; b) S. Feast, M. Englisch, A. Jentys, J. A. Lercher, *Appl. Catal. A* **1998**, *174*, 155; c) F. B. Passos, D. A. G. Aranda, R. R. Soares, M. Schmal, *Catal. Today* **1998**, *43*, 3.

[6] M. Haruta, N. Yamada, T. Kobayashi, S. Iijima, *J. Catal.* **1989**, *115*, 301.

[7] a) S. Tsubota, M. Haruta, T. Kobayashi, A. Ueda, Y. Nakahara, *Stud. Surf. Sci. Catal.* **1991**, *63,* 695; b) G. C. Bond, D. T. Thompson, *Catal. Rev. Sci. Eng.* **1999**, *319*, 388.

[8] a) M. Okumura, K. Tanaka, A. Ueda, M. Haruta, *Solid State Ionics* **1997**, *95*, 143; b) M. Okumura, S. Tsubota, M. Iwamoto, M. Haruta, *Chem. Lett.* **1998**, 315.

[9] V. Suryanarayanan, A. S. Nair, R. T. Tom, T. Pradeep, *J. Mater. Chem.* **2004**, *14*, 2661.

[10] P. D. Cozzoli, R. Comparelli, E. Fanizza, M. L. Curri, A. Agostiano, D. Laub, *J. Am. Chem. Soc.* **2004**, *126*, 3868.

[11] a) C. T. Kresge, M. E. Leonowicz, W. J. Roth, J. C. Vartuli, J. S. Beck, *Nature* **1992**, *359*, 710; b) J. S. Beck, J. C. Vartuli, W. J. Roth, M. E. Leonowicz, C. T. Kresge, K. D. Schmitt, C. T. W. Chu, D. H. Olson, E. W. Sheppard, S. B. McCullen, J. B. Higgings, J. L. Schlenker, *J. Am. Chem. Soc.* **1992**, *114*, 10834.

[12] a) P. Yang, T. Deng, D. Zhao, P. Feng, D. Pine, B. F. Chmelka, G. M. Whitesides, G. D. Stucky, *Science* **1998**, *282*, 2244; b) S. Y. Choi, M. Mamak, N. Coombs, N. Chopra, G. A. Ozin, *Adv. Funct. Mater.* **2004**, *14*, 335; c) E. L. Crepaidi, G. J. de A. A. Soler-lllia, D. Grosso, F. Cagnol, F. Ribot, C. Sanchez, *J. Am. Chem. Soc.* **2003**, *125*, 9770; d) M. Antonietti, G. A. Ozin, *Chem. Eur. J.* **2004**, *10*, 28.

[13] a) S. Kapoor, *Langmuir* **1999**, *15*, 4365; b) Y. Li, M. A. El-Sayed, *J. Phys. Chem. B* **2001**, *105*, 8938; c) R. Narayana, M. A. El-Sayed, *J. Am. Chem. Soc.* **2003**, *125*, 8340; d) N. R. Jana, Z. L. Wang, T. Pal, *Langmuir* **2000**, *16*, 2457; e) G. Schmid, H. West, H. Mehles, A. Lehnert, *Inorg. Chem.* **1997**, *36*, 891.

[14] a) A. Hagfeldt, M. Grätzel, *Acc. Chem. Res.* **2000**, *33*, 269; b) Q. H. Yang, M. P. Kapoor, S. Inagaki, *J. Am. Chem. Soc.* **2002**, *124*, 9694.

[15] J. C. Yu, X. C. Wang, L. Wu, W. K. Ho, L. Z. Zhang, G. T. Zhou, *Adv. Funct. Mater.* **2004**, *14,* 1178.

[16] a) L. H. Thompson, L. K. Doraiswamy, *Ind. Eng. Chem. Res.* **1999**, *38*, 1215; b) K. S. Suslick, G. J. Price, *Annu. Rev. Mater. Sci.* **1999**, *29*, 295.

[17] A. Gedanken, X. Tang, Y. Wang, N. Perkas, Y. Koltypin, M. V. Landau, L. Vradman, M. Herskowitz, *Chem. Eur. J.* **2001**, *7*, 4546.

[18] C. A. Alberius, K. L. Frindell, R. C. Hayward, E. J. Kramer, G. D. Stucky, B. F. Chmelka, *Chem. Mater.* **2002**, *14*, 3284.

[19] B. D. Cullity *Elements of X-ray Diffraction,* Addison-Wesley, London, **1978**, Chapter 1, pp. 101.

[20] S. J. Gregg, K. S. W. Sing, *Adsorption, Surface Area and Porosity*, Academic Press, London, **1997**, pp. 111–194.

[21] L. X. Zhang, J. L. Shi, J. Yu, Z. L. Hua, X. G. Zhao, M. L. Ruan, *Adv. Mater.* **2002**, *14*, 1510.

[22] a) J. F. Moulder, W. F. Stickle, P. E. Sobol, K. D. Bomben, *Handbook of X-ray Photoelectron Spectroscopy* (Ed.: J. Chastain), Perkin–Elmer Corporation, USA, **1992**, p. 182; b) D. Briggs, M. P. Seah, *Practical Surface Analysis*, *Vol. 1*, 2nd ed., Wiley, New York, **1993**.

[23] a) K. S. Suslick, T. W. Hyeon, M. M. Fang, *Chem. Mater.* **1996**, *8*, 2172; b) V. G. Pol, A. Gedanken, J. Calderon-Moreno, *Chem. Mater.* **2003**, *15*, 1111; c) K. S. Suslick, S. B. Choe, A. A. Cichowals, M. W. Grinstaff, *Nature* **1991**, *353*, 414.

[24] a) C. Mottet, G. Treglia, B. Legrand, *Surf. Sci.* **1996**, *675*, 352; b) J. Radnik, C. Mohr, P. Claus, *Phys. Chem. Chem. Phys.* **2003**, *5*, 172.

[25] J. Silvestre-Albero, A. Sepulveda-Escribano, F. Rodriguez-Reinoso, J. A. Anderson, *J. Catal.* **2004**, *223*, 179.

[26] C. Mottet, G. Treglia, B. Legrand, *Surf. Sci.* **1996**, *675*, 352.

[27] a) K. D. Schierbaum, S. Fischer, M. C. Torquemada, J. L. de Segovia, E. Roman, J. A. Martin-Gago, *Surf. Sci.* **1996**, *345*, 261; b) K. D. Schierbaum, X. W. Xing, S. Fischer, W. Göpel, in *Adsorption on Ordered Surfaces of Ionic Solids and Thin Films, Springer Series in Surface Science*, *Vol. 33* (Eds.: E. Umbach and H. J. Freund), Springer, Berlin, **1993**, p. 268.

[28] T. Saito, T. Iwase, J. Horie, T. Morioka, *J. Photochem. Photobiol. B* **1992**, *14*, 369.

[29] L. Z. Zhang, J. C. Yu, H. Y. Yip, Q. Li, K. K. Kwong, A. W. Xu, P. K. Wong, *Langmuir* **2003**, *19*, 10372.

[30] Z. Huang, P. C. Maness, D. M. Blake, E. J. Wolfrum, S. L. Smolinski, W. A. Jacoby, *J. Photochem. Photobiol. A* **2000**, *130*, 163.

[31] J. C. Yu, X. C. Wang, X. Z. Fu, *Chem. Mater.* **2004**, *16*, 1523.

Received: December 6, 2004
Published online: March 10, 2005